



# Free fall drag estimation of small-scale multirotor unmanned aircraft systems using computational fluid dynamics and wind tunnel experiments

T. Hammer<sup>1</sup> · J. Quitter<sup>1</sup> · J. Mayntz<sup>1</sup> · J.-M. Bauschat<sup>1</sup> · P. Dahmann<sup>1</sup> · F. Götten<sup>2</sup> · S. Hille · E. Stumpf<sup>3</sup>

Received: 11 February 2023 / Revised: 8 November 2023 / Accepted: 9 November 2023 / Published online: 12 December 2023  
© The Author(s) 2023

## Abstract

New European Union (EU) regulations for UAS operations require an operational risk analysis, which includes an estimation of the potential danger of the UAS crashing. A key parameter for the potential ground risk is the kinetic impact energy of the UAS. The kinetic energy depends on the impact velocity of the UAS and, therefore, on the aerodynamic drag and the weight during free fall. Hence, estimating the impact energy of a UAS requires an accurate drag estimation of the UAS in that state. The paper at hand presents the aerodynamic drag estimation of small-scale multirotor UAS. Multirotor UAS of various sizes and configurations were analysed with a fully unsteady Reynolds-averaged Navier–Stokes approach. These simulations included different velocities and various fuselage pitch angles of the UAS. The results were compared against force measurements performed in a subsonic wind tunnel and provided good consistency. Furthermore, the influence of the UAS's fuselage pitch angle as well as the influence of fixed and free spinning propellers on the aerodynamic drag was analysed. Free spinning propellers may increase the drag by up to 110%, depending on the fuselage pitch angle. Increasing the fuselage pitch angle of the UAS lowers the drag by 40% up to 85%, depending on the UAS. The data presented in this paper allow for increased accuracy of ground risk assessments.

**Keywords** Multirotor UAS · Drag estimation · CFD · Wind tunnel experiments · Wind milling

## Abbreviations

CAD	Computer-aided design	RAD	Rotor axis distance
CFD	Computational fluid dynamics	RANS	Reynolds-averaged Navier–Stokes
EU	European union	RPM	Revolutions per minute
FP	Fixed propellers	SIMPLE	Semi-implicit method for pressure linked equations
GRC	Ground risk class	SORA	Specific operations risk assessment
IR	Implementing regulations	SP	Spinning propellers
MS	Mounting system	UAS	Unmanned aircraft system
MTOM	Maximum take-off mass	WT	Wind tunnel

✉ T. Hammer  
thorben.hammer@alumni.fh-aachen.de

J. Quitter  
quitter@fh-aachen.de

J. Mayntz  
mayntz@fh-aachen.de

J.-M. Bauschat  
bauschat@fh-aachen.de

P. Dahmann  
dahmann@fh-aachen.de

F. Götten  
falk.goetten@lba.de

S. Hille  
sebastian.hille@ilr.rwth-aachen.de

E. Stumpf  
eike.stumpf@ilr.rwth-aachen.de

<sup>1</sup> Department of Aerospace Engineering, FH Aachen University of Applied Science, 52064 Aachen, Germany

<sup>2</sup> Referat B5 Unmanned Aerial Systems, Luftfahrt Bundesamt, 38108 Braunschweig, Germany

<sup>3</sup> Institute of Aerospace Systems, RWTH Aachen University, 52062 Aachen, Germany

## 1 Introduction

The increasing number of unmanned aircraft systems (UAS), especially small-scale multirotor UAS, necessitates the introduction of new safety regulations. New regulations were introduced in recent years and the existing ones were revised. Currently, the European regulations for UAS and the corresponding operations are defined in the Implementing Regulations (IR) (EU) 2019/947 [1]. Operations with UAS are subdivided into different categories. In the specific category, UAS operations require an operational authorisation according to Article 12 of the regulations mentioned before.

For authorisation, an operational risk assessment is necessary. This risk assessment can be conducted using the specific operations risk assessment (SORA). One part of the SORA process is determining the ground risk class (GRC). The ground risk is related to the risk harming people on the ground in case of UAS failure. For the determining the ground risk, UAS operations are classified depending on the kinetic impact energy of the UAS hitting the ground and on the operational scenario.

The kinetic impact energy depends heavily on the aerodynamic drag of the UAS. There are only little data about the drag of multirotor UAS. First assumptions could be found in Hwang et al. [2] and Bannwarth et al. [3]. However, no data for a wide range of small-scale multirotor UAS are available.

This research aims to generate aerodynamic drag coefficients, representing a wide range of currently used multirotor UAS. Furthermore, investigating different influencing parameters on the free fall drag is pursued.

### 1.1 Physical background on free falling UAS

The influence of the UAS drag on the free fall behaviour is demonstrated with a comparison between the two cases of neglecting and including the aerodynamic drag. Furthermore, various drag coefficients were considered to show the importance of the correct value. Parameters from an artificial UAS were taken and inserted into the corresponding formulas. For all computations, mean sea-level

**Table 1** Parameters to represent the free fall behaviour

Parameter	Value
Air density, kg/m <sup>3</sup>	1.225
Gravitational acceleration, m/s <sup>2</sup>	9.81
Mass of the UAS, kg	2.5
Reference area of the UAS, m <sup>2</sup>	0.2

conditions are assumed and the air density is constant for all altitudes. Table 1 shows these parameters.

In the absence of aerodynamic drag and under identical gravitational conditions, every object has the same free fall behaviour. The red dotted line in Fig. 1 shows the free fall velocity over the falling height without aerodynamic drag. The free fall velocity for the artificial UAS with drag is displayed for a drag coefficient ( $c_D$ ) of 0.3, 0.4 and 0.5 using dashed and dashed-dotted lines.

For the free falling UAS with drag, the velocity increases until the terminal velocity is reached. At this stage, the gravitational and the aerodynamic drag force are identical but acting in opposite directions. Therefore, the UAS is no longer accelerated. Comparing the behaviour of any object during free fall excluding the aerodynamic drag, with the behaviour of the UAS including aerodynamic drag, results in a significant mismatch between the two. For a free fall from 75 m, any object without aerodynamic drag has an impact velocity of 38 m/s, while the UAS with a drag coefficient of 0.3 has an impact velocity of 24 m/s. This difference in velocity results in a 155% difference in the kinetic impact energy. Hence, including the aerodynamic drag in the free fall estimation is necessary to compute accurate results. Due to that, this publication presents the applied methodology to estimate aerodynamic drag coefficients of multirotor UAS and the corresponding results of the investigated UAS.

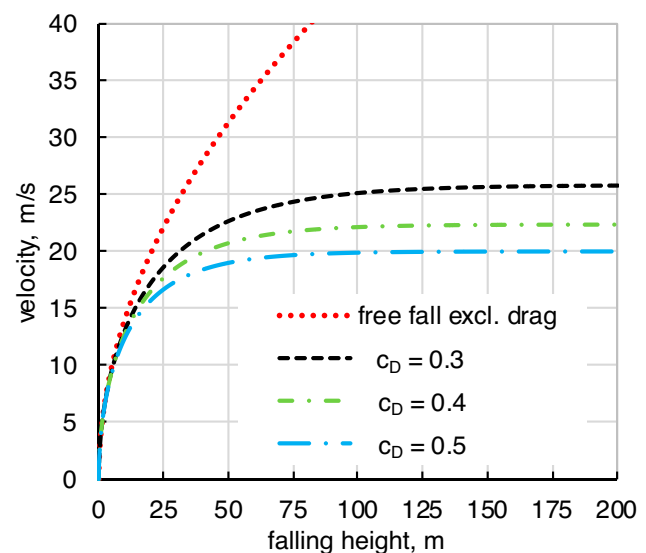


**Fig. 1** Free fall behaviour with various drag coefficients

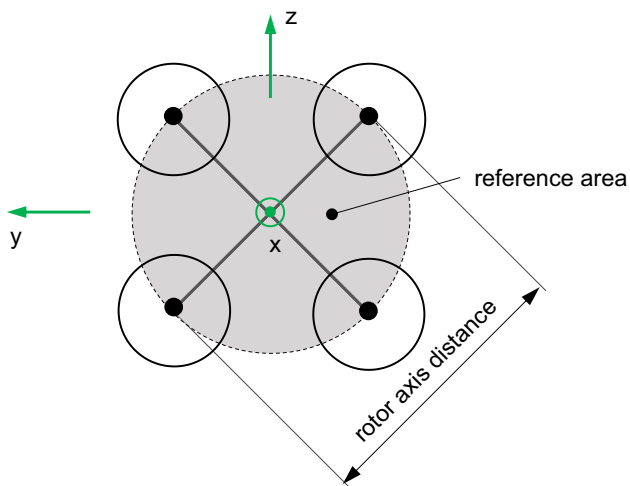


**Fig. 2** Definition of the reference area and the body-fixed coordinate system in a top view

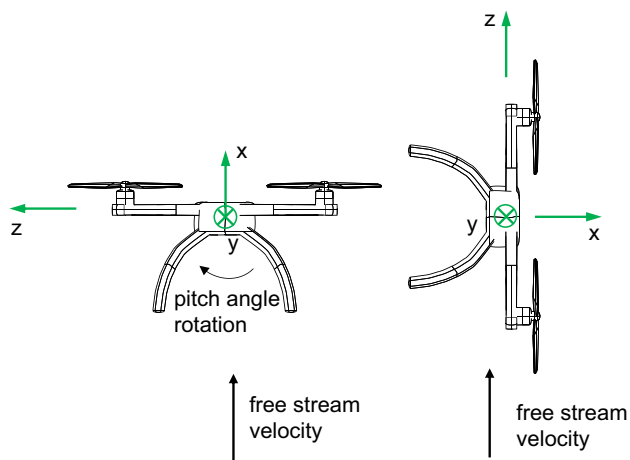


**Fig. 3** Definition of the fuselage pitch angle rotation; left  $0^\circ$  and right  $90^\circ$

## 2 Methodology

### 2.1 UAS geometry selection and modelling

Computation of a drag coefficient requires a corresponding reference area. Standardized reference areas for multirotor UAS are not yet consistently defined in the literature. In this study, the reference area is defined as the area of a circle passing through all rotor axes.

The defined reference area is shown in Fig. 2 with the grey area for an exemplary multirotor UAS. The diameter of this circle is defined as the rotor axis distance (RAD). In addition, the body-fixed coordinate system is shown as well.

In Fig. 3, the fuselage pitch angle definition used for all simulations is shown. The fuselage pitch angle rotation is defined as a rotation around the body-fixed y-axis, while the incoming flow is in line with the x-axis for  $0^\circ$  fuselage pitch angle.

The investigated UAS were chosen based on an in-house database, which includes over 100 UAS. This database includes the general geometrical dimensions, the UAS weights and flight performance parameters if available. Only a few UAS came with detailed information about the geometrical shape of the UAS. Therefore, the 3D models were rebuilt based on three view images, open CAD models, and the geometrical dimensions from the database. Missing geometrical dimensions were extrapolated from the existing dimensions with isometric and three side scaled views of the UAS.

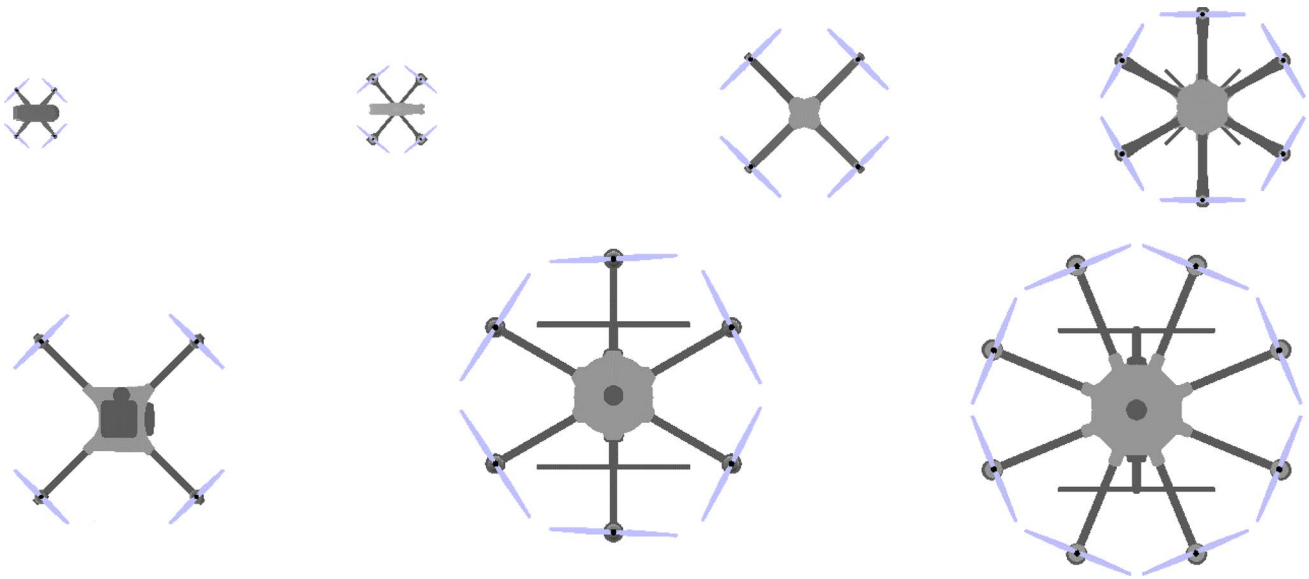
From the database, seven UAS were selected as being representative for a wide range of currently used multirotor UAS. A scaled top view of each analysed UAS is shown in Fig. 4. All UAS are shown with an unscaled, isometric view in Fig. 5.

Table 2 displays the most important parameters of each UAS, including the projected area of each UAS seen in the top view.

The geometrical models were rebuilt using the NASA Tool OpenVSP in version 3.25 [4]. The 3D models for the CFD simulations contain all parts of the UAS except externally mounted batteries, motor controllers, cables and video cameras. All holes in the frame of the UAS were filled to reduce the complexity of the 3D models. Furthermore, all geometrical models have fixed propellers, so no rotational effects are considered in the CFD results. A common, representative propeller blade geometry was used for all UAS and scaled accounting for the size difference of the UAS. For all fixed propellers simulations and experiments the propellers of all UAS were orientated perpendicular to the arms.

### 2.2 Simulation approach

All CFD simulations were performed using the computational fluid dynamics software from Siemens StarCCM+ v15.02.007. This software has been successfully employed and the general simulation approach was validated for UAS drag estimation by Götten [5], and flight mechanical derivative estimation from Quitter et al. [6]. The air flow is modelled as a continuous medium via the Navier–Stokes equations. These equations were simplified to Reynolds-averaged Navier–Stokes (RANS) equations to run time efficient solutions with adequate accuracy. Menter's Shear Stress Transport model serves as the turbulence model. It combines the  $k$ - $\omega$ -model for the near-wall flow and the  $k$ - $\epsilon$ -model for turbulence effects in the free stream. A quadratic, non-linear constitutive relationship was used



**Fig. 4** Top view of all UAS; UAS 1 to UAS 7 from top left to bottom right (scaled view)

for computing the turbulent viscosity as recommended by Spalart [7]. The unsteady RANS equations are solved based on the Semi-Implicit Method for Pressure Linked Equations (SIMPLE) algorithm. Compressible effects are not expected in the used velocity regimes. Initial time stepping parameters were specified and updated during a process by lowering the time step. Then, the simulation was run until a physical time of 0.5 s was reached with time steps of  $5 \cdot 10^{-4}$  s. Aerodynamic forces are calculated from a surface pressure and shear stress integral. The drag force is the aerodynamic force vector in flow direction. Drag coefficients were averaged for the last 100 iterations of each unsteady solution. Within these results, the fluctuations of the results are reduced to an order of magnitude of  $1 \cdot 10^{-4}$  for the drag coefficients.

For the simulation domain, a bullet-shaped flow field with a diameter of 50 m and an overall length of 75 m was used (Fig. 6). The used parameters of the flow domain were extrapolated and adapted from the suggestions given by Götten [5] for the used methodology.

At the curved inlet, the velocity direction and magnitude, pressure, and turbulence parameters are specified. To prevent a numerical variation of the specified turbulence parameters over the length of the domain, a ‘control decay’ was used as recommended by Götten [5] and is described in detail by Spalart et al. [8]. At the outlet, the pressure is set to a specific value, while the velocity is calculated downstream of the domain. The specified values for the simulations are mean sea-level conditions and are shown in Table 3. Within the study, the velocity was varied between several values to ensure that all results were velocity independent.

The whole simulation domain was discretised using the current state of the art finite-volume method described by

Laurien et al. [9]. The meshes contain unstructured polyhedral cells to discretise arbitrary complex geometries. Polyhedral cells benefit from a fast information transfer through the domain, because of the increased number of faces compared to quadratic cells as stated by Götten [5]. A non-homogenous mesh was used to increase time-efficiency. Mesh refinements were individual applied for all UAS depending on their sizes and were done to all UAS surfaces, edges and to the nearfield around the UAS. Particular care was taken to the mesh refinement of the wake. The initial wake refinement was defined as a cylinder with a diameter 1.3 times the largest dimension of the UAS and was updated based on simulation results after a number of iterations. The boundary layer was discretised using a specific 25 cell prism layer mesh. The near-wall thickness is selected to reach a  $y^+$  value smaller 1 at each wall. A smooth transition between different meshes and different cell sizes was ensured to increase the overall mesh quality. Figure 7 show the surface mesh of UAS 3 in detail.

A mesh metrics study was conducted to verify that the meshes and the refinements are sufficient and that the simulation results do not differ with an increased cell count. During this study, the overall drag and the drag for the individual components of the UAS were monitored. Figure 8 show the total drag coefficient of UAS 3 as a function of the cell count exemplarily.

For simulations with meshes smaller than 13 Mio cells, the overall drag varies with the number of cells. Increasing the number of cells beyond 13 Mio cells does not change the drag coefficient considerably. Due to that, for UAS 3 only simulations with 18.6 Mio cells were used.

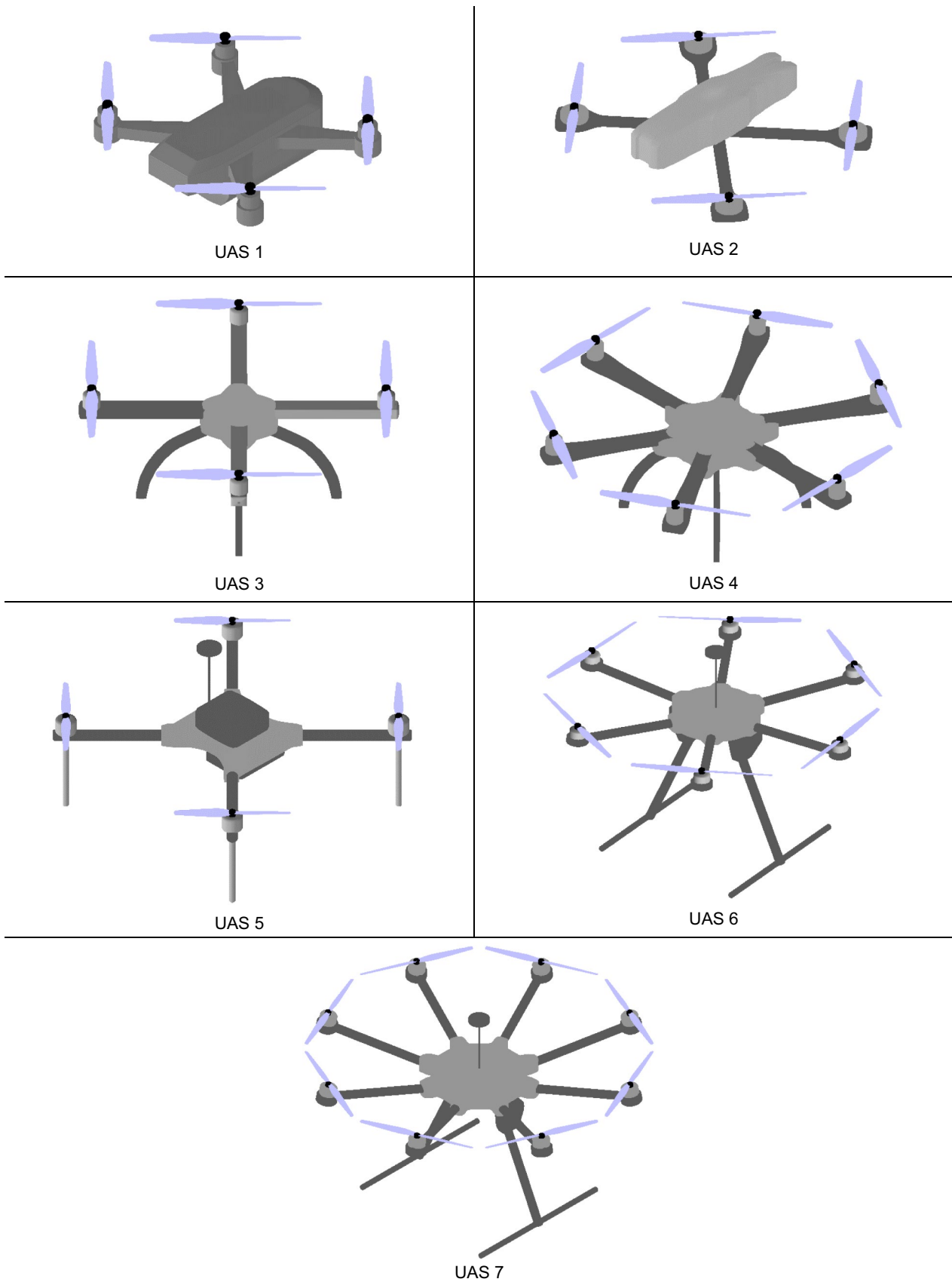
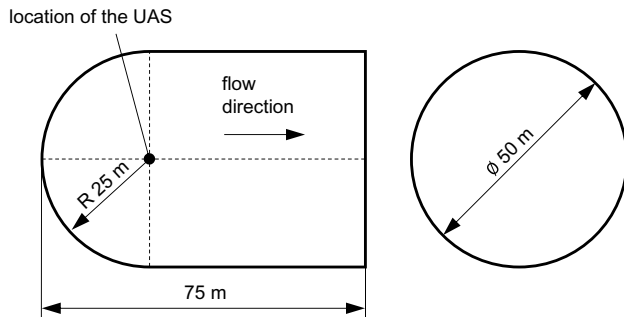


Fig. 5 Isometric view of all analysed UAS (size not to scale)

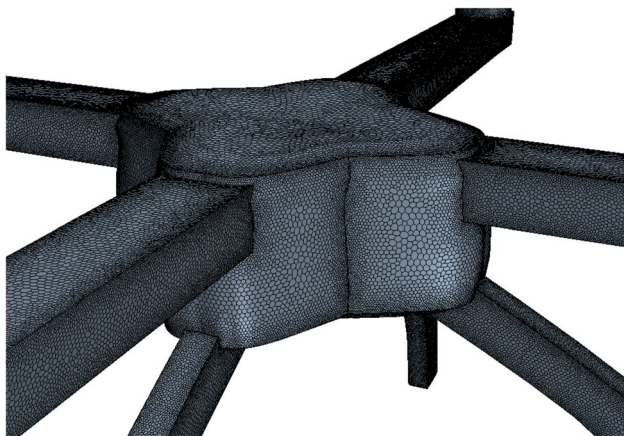
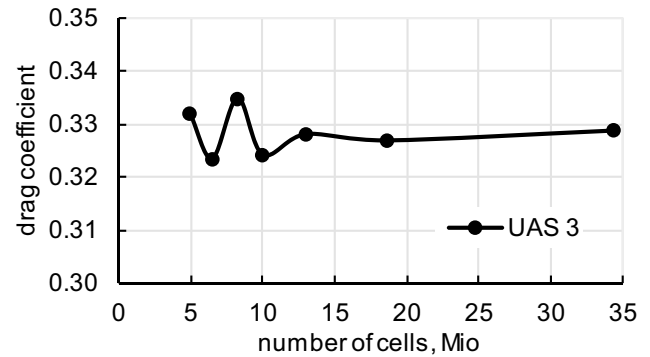


**Table 2** General data of the investigated UAS

UAS, No	MTOM, kg	$S_{ref}$ , m <sup>2</sup>	Projected area, m <sup>2</sup>
1	0.3	0.0241	0.0120
2	0.75	0.0401	0.0147
3	1.6	0.1590	0.0408
4	2.4	0.2376	0.0824
5	3.6	0.3318	0.0667
6	8.2	0.5931	0.1445
7	11	0.7574	0.2006

**Fig. 6** Bullet-shaped simulation domain**Table 3** Boundary conditions for all CFD simulations

Parameter	Value
Pressure, Pa	101,325
Air density, kg/m <sup>3</sup>	1.225
Dynamic viscosity, Pa·s	$1.789 \cdot 10^{-5}$
Temperature, K	288.15
Turbulence intensity	0.01
Turbulence viscosity ratio	5

**Fig. 7** Polyhedral surface mesh of UAS 3**Fig. 8** Overall drag in the mesh metrics study for UAS 3

All simulations were started as steady simulations. The initial iteration steps serve as the starting point for the unsteady simulations. After 3000 steady iteration steps, the simulations were switched from steady to unsteady. During the CFD investigations, all UAS were analysed with fixed propellers. CFD analysis with rotational propellers would have increased the computational effort extensively and were not feasible. Fuselage pitch angles from 0° to 180° in 30° steps were investigated. Simulations with different velocities were performed (Fig. 9) to investigate the influence of the velocity on the drag coefficients. This investigation shows the independence of the drag coefficients on free stream velocity under the conditions selected.

### 2.3 Wind tunnel experiments

The results from the CFD simulations are validated by a comparison to force measurements from a wind tunnel study conducted with two UAS. In addition, the wind tunnel tests were done to evaluate the influence of free spinning propellers on the overall drag of a UAS. A subsonic wind tunnel located at the RWTH Aachen University was chosen for these investigations, as the authors had prior experience with the facility from previous projects as described by Mayntz et al. [10]. It is a closed-loop (Göttingen type) wind tunnel and operates under atmospheric conditions (Fig. 10).

The drive train allows free stream velocities of up to 70 m/s and the wind tunnel has a degree of turbulence of 2.5%.

Within the study, real versions of UAS 3 and 4 were investigated in the wind tunnel. All electronics neglected in the CFD models were removed from the UAS to keep both studies comparable. The models were mounted to a six-component strain gauge wind tunnel scale with a 3D printed adapter (Fig. 11). During the experiments, the measurement system calculates static mean values from 500 samples taken in 1 s. The complete measurement system was corrected for the gravitational forces of the models and the mounting systems.

**Fig. 9** Drag coefficient over free stream velocities for UAS 3 with  $0^\circ$  fuselage pitch angle

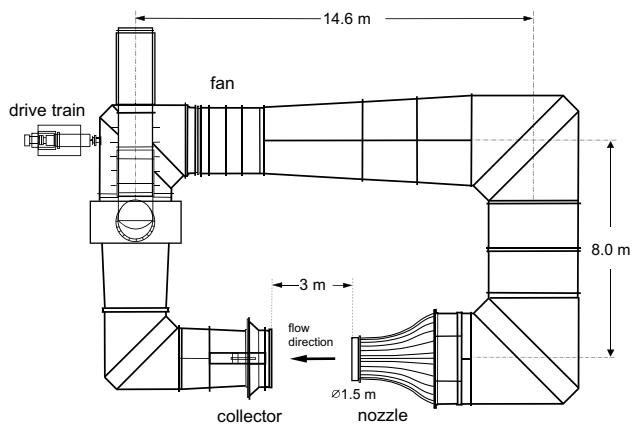
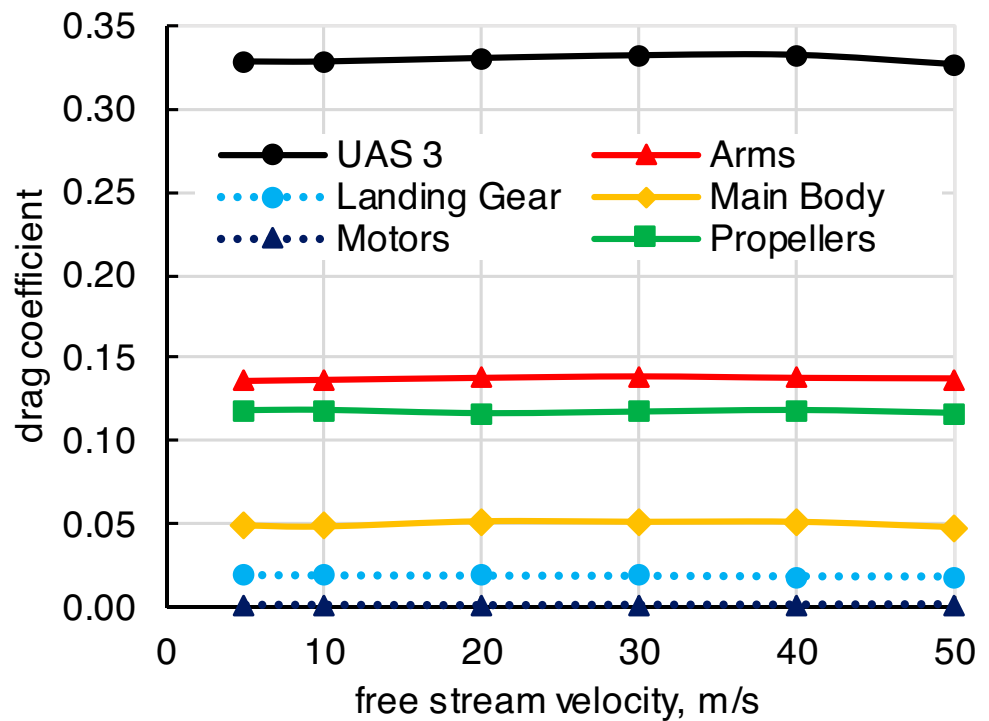


**Fig. 10** Schematic sketch of the subsonic, closed-loop, free jet wind tunnel

Throughout the measurements, the two UAS were investigated with fuselage pitch angles from  $0^\circ$  to  $90^\circ$  in  $5^\circ$  steps. First the UAS were investigated with fixed propellers. According to the CFD simulations, the propellers were orientated perpendicular to the arms. In a second study, both UAS were investigated with free spinning propellers. The UAS and the measurement system were mounted on the facility's actuated model mount (Fig. 12) to adjust different fuselage pitch angles. This device ensures that the UAS always rotates around its own centre, so that the UAS always stays in the core of the free stream.

With an increasing fuselage pitch angle of the UAS, the mounting system steps out behind the UAS in the free

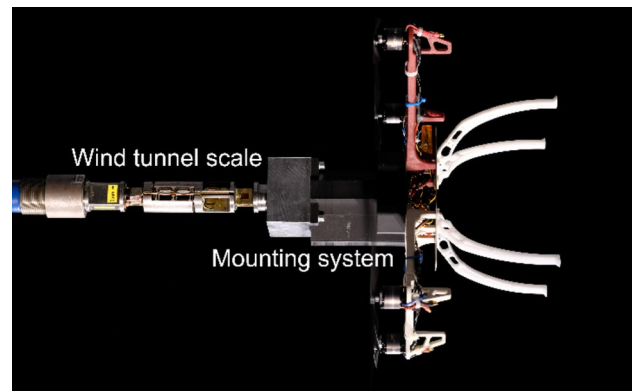


**Fig. 11** UAS 3 mounted on the wind tunnel scale

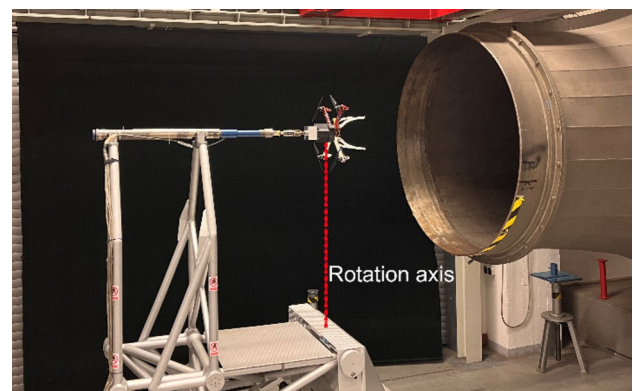


**Fig. 12** UAS 3 positioned in the wind tunnel by the actuated model mount

stream. This affects the force measurements with its own aerodynamic drag. A post processing correction was applied, to avoid this error

$$c_{d,corr}(\theta) = c_{d,UAS}(\theta) - \sin(\theta) \cdot c_{d,MS}(\theta). \quad (1)$$

The corrected drag coefficient is calculated with the initially measured drag coefficient of the UAS including the mounting system ( $c_{d,UAS}$ ). In a separate measurement, the aerodynamic drag of the mounting system ( $c_{d,MS}$ ) is determined for all investigated fuselage pitch angles ( $\theta$ ) and then subtracted with a sine function from the initially measured drag coefficient, to account for the mounting system being exposed to the free stream at increased fuselage pitch angles (Eq. (1)). The applied method can be a reason for errors during the evaluation, however it was used due to a lack of alternatives and was not further investigated during the research.

As with the CFD simulations, the drag coefficients' velocity independence was also confirmed (Fig. 13).

### 3 Results

In this section, the results from the CFD simulations and the wind tunnel study are presented. First, an overview of the pressure coefficient combined with streamlines around the UAS from the CFD simulation is given for all UAS surfaces.

Stagnation conditions are only found at surfaces perpendicular to the free stream and are displayed in red colour in Fig. 14. The rectangular arms show a larger area of positive pressure coefficient than the tubular arms. This explains the increased drag for UAS with rectangular arms.

#### 3.1 Drag coefficients

Initial calculations with drag coefficients showed that the terminal velocity of all investigated UAS is approximately

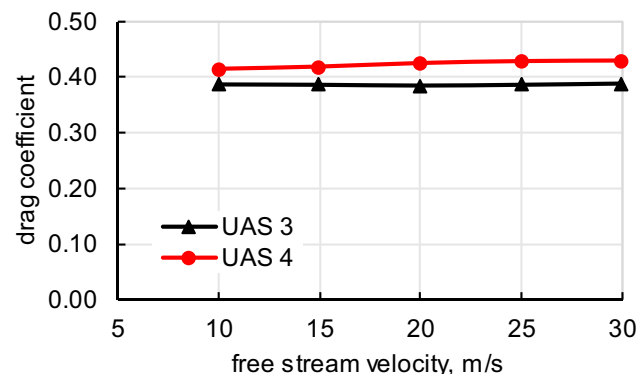


**Fig. 13** Evaluated drag coefficient over free stream velocity in the wind tunnel

20 m/s under the used conditions. Therefore, all presented results are from CFD simulations with an inlet velocity of 20 m/s and fixed propellers. The drag coefficients of all investigated UAS are shown in Fig. 15 for 0° fuselage pitch angle.

A general correlation between the size of the UAS and the drag coefficient could not be found for the investigated velocity regimes. This indicates that the reference area is well selected, because the drag coefficient does not depend on the actual size of the UAS.

In general, the UAS with rectangular-shaped arms show a higher drag compared to UAS with tubular-shaped arms. Investigating a drag breakdown of the UAS by components shows that the arms of an UAS are the component with the largest aerodynamic drag contribution (Fig. 16).

Exemplarily, a drag breakdown of UAS 3 is shown in Fig. 16. The other UAS show very similar contributions of the components.

A comparison between the CFD results and the measured results from the wind tunnel study is presented in Fig. 17 for 0° fuselage pitch angle.

UAS 3 has a difference of 18% between the wind tunnel study and the CFD simulation, while the difference for UAS 4 is only 2%. The difference can result from the difference between the 3D models and the real UAS, especially from the different propeller blades. UAS 3 and 4 had different propellers mounted with different blades, while the 3D models were equipped with a universal propeller. However, the wind tunnel study's drag coefficients and CFD simulations show good agreement. This indicates that the CFD simulations deliver reasonable results for aerodynamic drag coefficients of multirotor UAS, especially considering that the models tested in the wind tunnel are actual UAS.

#### 3.2 Fuselage pitch angle sweep

As mentioned before, investigations with different fuselage pitch angles of the UAS were done in the wind tunnel study as well as in the CFD simulations. The definition of the fuselage pitch angle and the corresponding rotation can be found in Fig. 3.

Initial CFD investigations with fuselage pitch angles between 0° and 180° show a symmetric behaviour of the drag coefficients for fuselage pitch angles larger than 90°. Therefore, the time-consuming, unsteady simulations were only conducted for fuselage pitch angles of up to 90°. The drag behaviour with different fuselage pitch angles for UAS 3 and each component is shown in Fig. 18.

The overall drag decreases with an increasing fuselage pitch angle. All UAS show the lowest drag coefficient at a fuselage pitch angle of 90° and the largest drag coefficient at a fuselage pitch angle of 0°. This behaviour differs for the individual components of the UAS. For UAS 3, 4 and



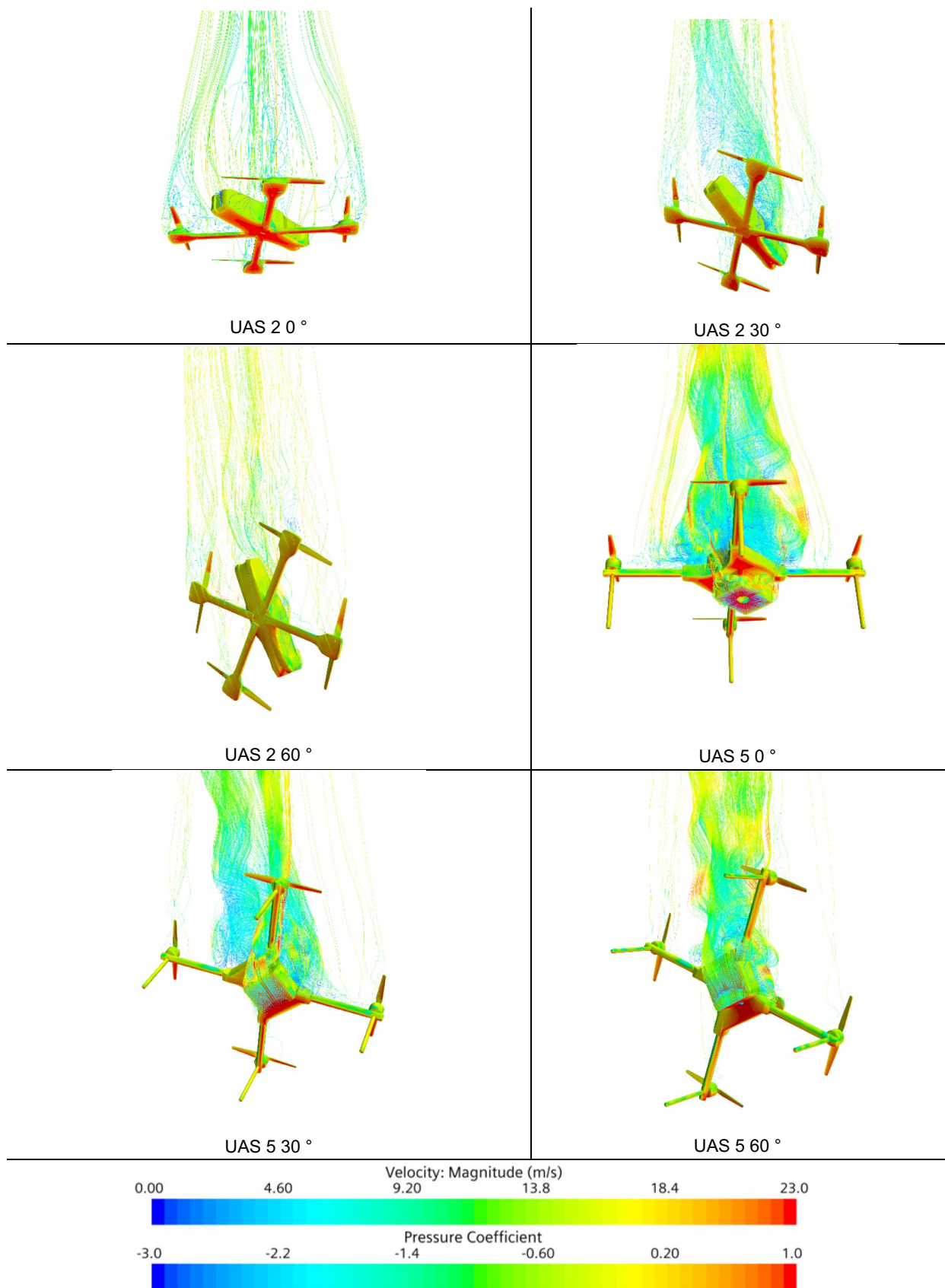


Fig. 14 Isometric view of pressure coefficients on the UAS surfaces and streamlines for various fuselage pitch angles (size not to scale)

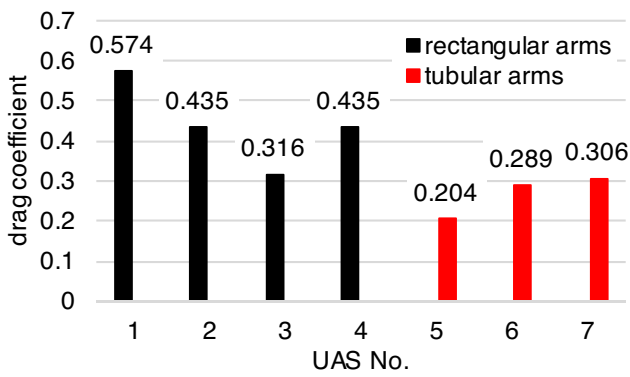


Fig. 15 Drag coefficients of all UAS from CFD simulations for 0° fuselage pitch angle

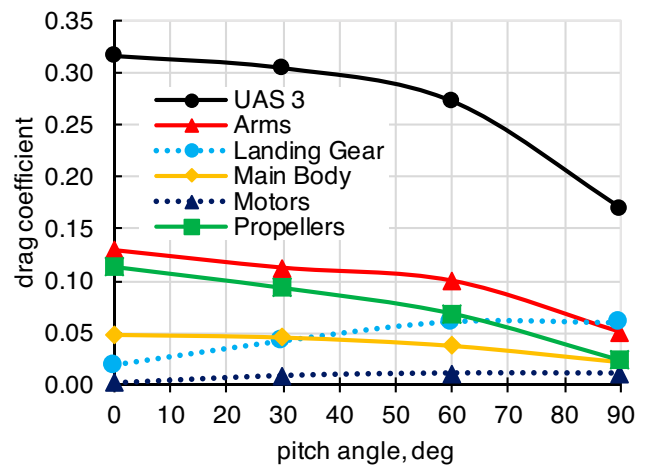


Fig. 18 CFD fuselage pitch angle sweep for UAS 3

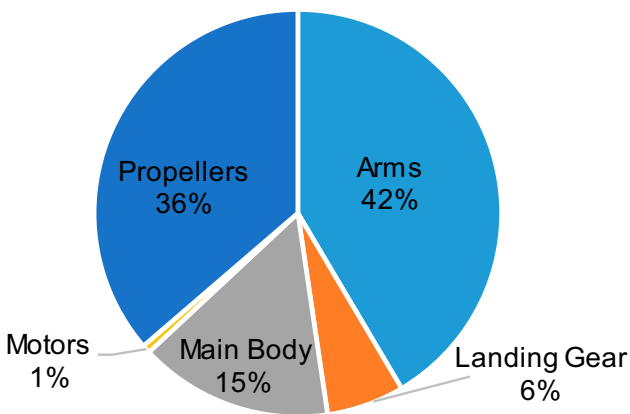


Fig. 16 Drag breakdown of each component of UAS 3 for 0° fuselage pitch angle

Table 4 Drag coefficients from CFD simulations of all investigated UAS

Fuselage pitch angle, deg	0	30	60	90
UAS 1	0.576	0.509	0.328	0.225
UAS 2	0.435	0.362	0.207	0.064
UAS 3	0.316	0.304	0.273	0.170
UAS 4	0.438	0.372	0.244	0.116
UAS 5	0.204	0.183	0.152	0.115
UAS 6	0.288	0.267	0.171	0.114
UAS 7	0.306	0.266	0.196	0.121

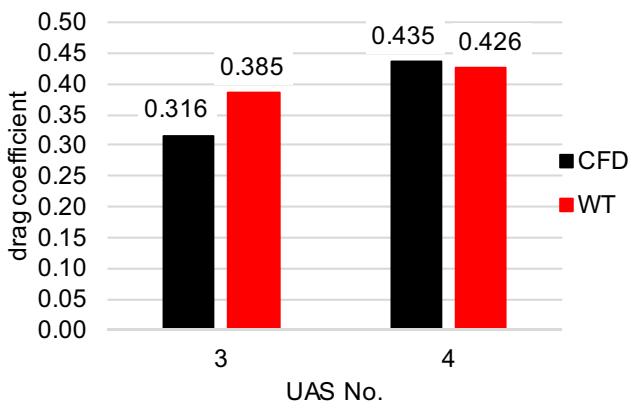


Fig. 17 Comparison between CFD simulations and wind tunnel (WT) measurements

5, the landing gear drag as well as the drag of the motors increases with the fuselage pitch angle. The same behaviour was observed for the landing gear drag of UAS 6 and

7, while the drag of the motors decreased for UAS 6 and 7 with an increasing fuselage pitch angle. These different behaviours result in individual curves for the overall drag of each UAS, depending on the percentual contribution of each UAS component on the overall drag. The total drag coefficients of all UAS evaluated in the CFD simulations are presented in Table 4.

During the wind tunnel study, all fuselage pitch angle investigations were done with several velocities. This has shown that the drag coefficient is not velocity-dependent with different fuselage pitch angles.

The following diagrams compare the CFD results of UAS 3 and UAS 4 with those from the wind tunnel study. The red graphs show the results from the CFD simulations and the black graph represents the wind tunnel (WT) results. The wind tunnel results are of a higher fuselage pitch angle resolution due to significantly reduced measurement time compared to the CFD analysis.

For UAS 3, both approaches differ a maximum of 18% at 0°, as already mentioned in chapter 3.1. With higher

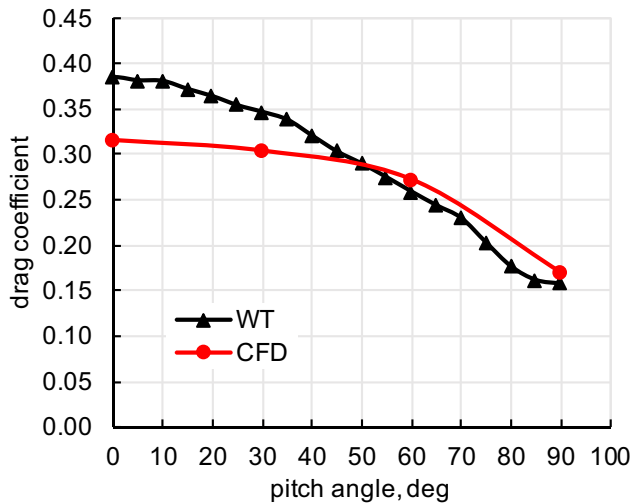


Fig. 19 Fuselage pitch angle sweep for UAS 3 in WT and CFD

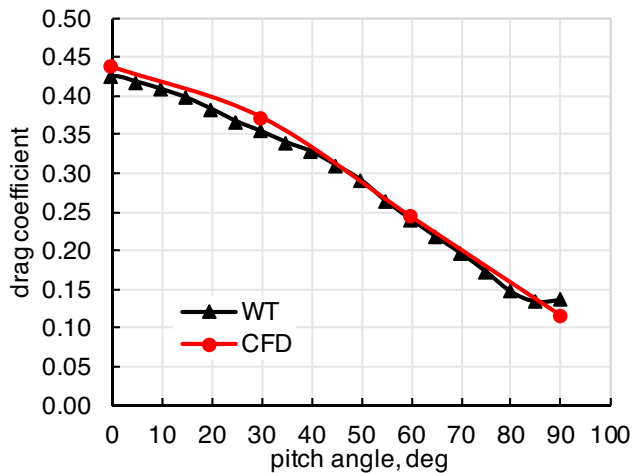


Fig. 20 Fuselage pitch angle sweep for UAS 4 in WT and CFD

fuselage pitch angles, both methods nearly match each other (Fig. 19).

The results from the CFD simulations and the wind tunnel tests match each other for UAS 4 for all fuselage pitch angles. Concluding the results from both UAS, the CFD simulations deliver accurate results for the aerodynamic drag of multirotor UAS at different fuselage pitch angles (Fig. 20).

### 3.3 Propeller influence on the aerodynamic drag

In the CFD investigations, only UAS with fixed propellers were investigated. Another common failure case for multirotor UAS is that the propellers are not locked by the motors and can spin freely. The computational effort in CFD of free spinning propellers is extensively higher compared to fixed propellers. Therefore, UAS with spinning propellers were

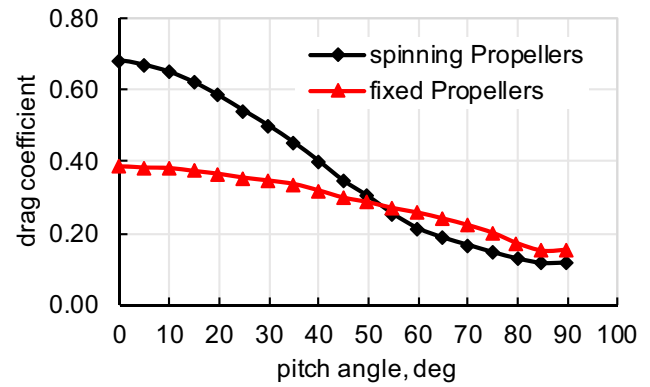


Fig. 21 Difference between fixed propellers and spinning propellers for UAS 3

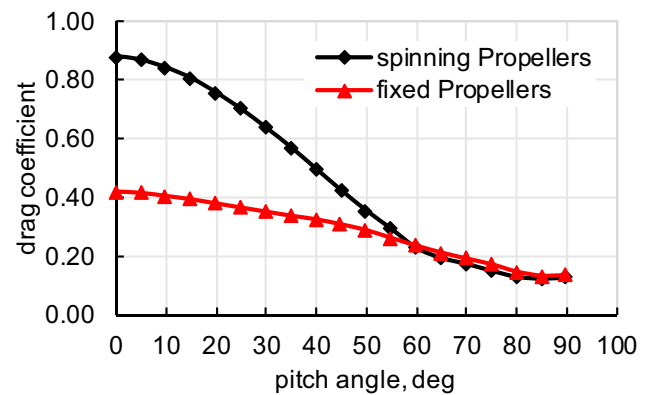


Fig. 22 Difference between fixed propellers and spinning propellers for UAS 4

only investigated in the wind tunnel study. Within the measurements with free spinning propellers, the velocity dependence of the drag coefficient was again investigated. Within meaningful velocities, the drag coefficient is independent of the free stream velocity. Care was taken, so that the maximum rotational speed of the propellers was not reached. The results shown were evaluated with a free stream velocity of 15 m/s. Figure 21 show the difference between fixed and spinning propellers for UAS 3.

At low fuselage pitch angles, the drag coefficients differ significantly. Free spinning propeller increases the total drag of the UAS by about 75%. A similar behaviour can be observed between wind milling and stationary propeller for aircrafts as described in Gudmundsson [11]. When increasing the fuselage pitch angle, the differences between both decrease until the drag matches at about 50°. During the wind tunnel tests, all propellers consistently spin at low fuselage pitch angles. With increasing fuselage pitch angle, the airflow through the propellers decreases, leading to lower rotor RPM for the free spinning propellers and at the end to stationary propellers. In general, the propellers stopped at fuselage pitch angles

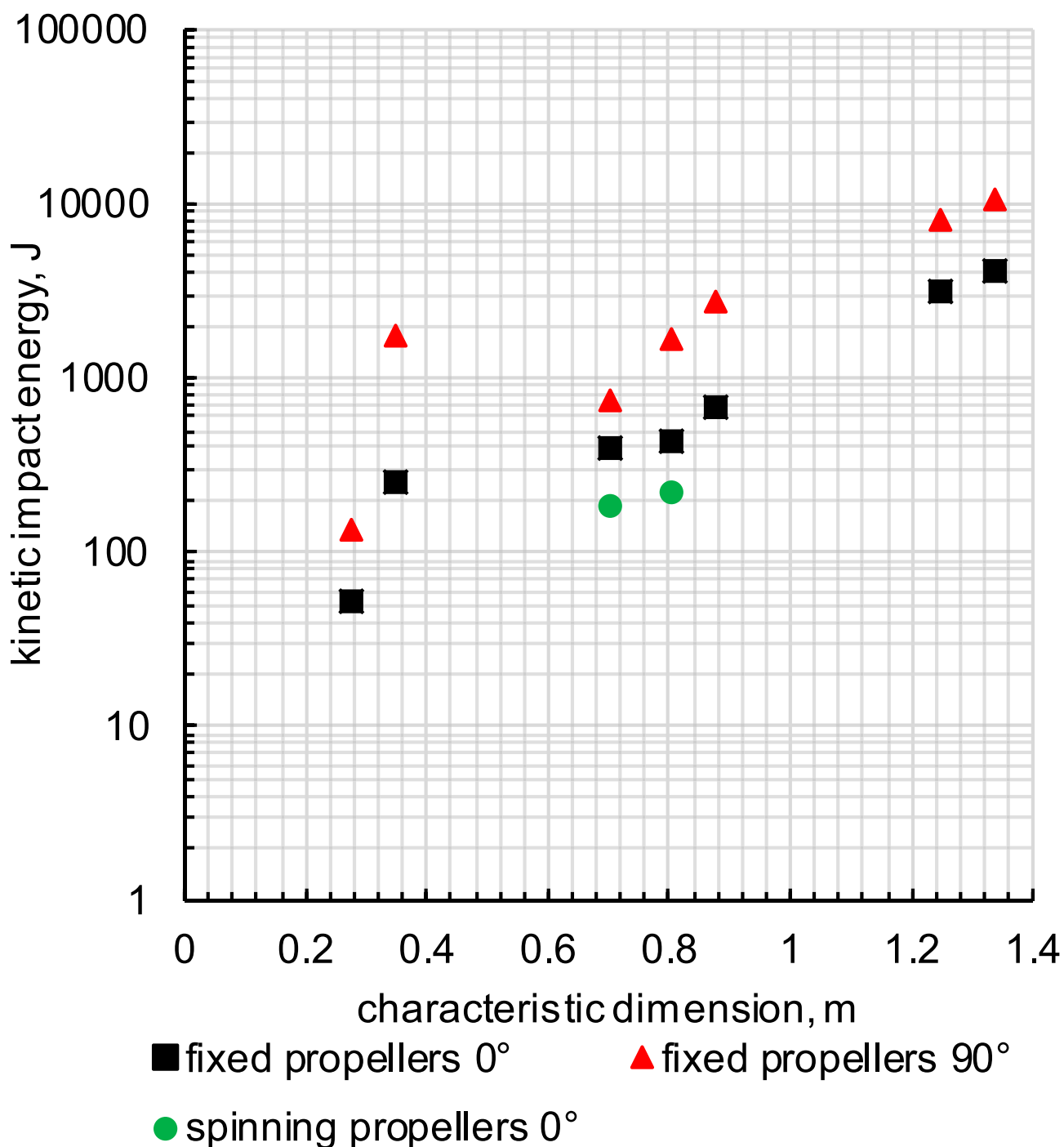


Fig. 23 Maximum kinetic impact energy for each UAS with the investigated conditions

between  $55^\circ$  and  $80^\circ$ . The exact fuselage pitch angle when the propeller stopped was depended on the UAS, the position of the propeller at the UAS and the free stream velocity. Due to that the graphs match each other at higher fuselage pitch angles. UAS 4 show a similar behaviour (Fig. 22).

Free spinning propellers increase the overall drag of UAS 4 at  $0^\circ$  by about 110% and the drag matches at fuselage pitch angles excess of  $55^\circ$ .

Two configurations tested show that each spinning rotor accounts for an extra drag of approximately 20% of the UAS drag with fixed propellers. Note that both UAS are of very similar construction.

The results show a significant difference between free spinning and fixed propellers for low fuselage pitch angles. Both UAS show significantly lower spinning propellers for all rotors at fuselage pitch angles of above  $55^\circ$ , leading to a small difference in the overall drag between free spinning and fixed propellers.

### 3.4 Free falling UAS including aerodynamic drag

With the evaluated drag coefficients, the free fall behaviour and, more importantly, the kinetic impact energy under the given conditions can be computed accurately. Therefore, an accurate ground risk class analysis is possible. During the SORA process, the UAS are classified by their characteristic dimension [1]. This dimension is the maximum dimension of a UAS. For multirotor UAS, it is, in most cases, the diagonal between the rotor axis plus one diameter of the propeller. Due to that, the presented results are shown here regarding their characteristic dimension.

In Fig. 23, the UAS are listed by their characteristic dimension from left to right. UAS 1 has the smallest characteristic dimension and UAS 7 the largest. The symbols for each UAS show the maximum and minimum expected kinetic impact energy. Two values for each UAS and an additional one for UAS 3 and 4. The top value corresponds to a free fall with a fuselage pitch angle of  $90^\circ$ , while the bottom value corresponds to a free fall with a fuselage pitch angle of  $0^\circ$ . The additional values for UAS 3 and 4 represent a free fall with spinning propellers and at  $0^\circ$  fuselage pitch angle. Therefore, this diagram presents a conservative range of possible kinetic impact energies when the terminal velocity has been reached. These values can be used for an accurate ground risk class investigation of the UAS for several operations.

## 4 Conclusion

In this paper, drag coefficients for several falling situations of various multirotor UAS are presented, so that the build-up of kinetic energy can be computed more accurately. During the research, CFD simulations were conducted and verified in wind tunnel experiments. Both methods' results match, indicating accurate results. The evaluation shows velocity independence of the drag coefficient for all investigated cases. A general correlation between the size of the UAS and the drag coefficient could not be found. This indicates that the rotor axis circle is a reasonably defined reference area for drag analysis of multirotor UAS. The fuselage pitch angle of the UAS during free fall has a significant influence on the drag, with drag coefficients decreasing by as much as 40% to 85% at  $90^\circ$  of fuselage pitch angle. The failure cases of the propulsion system have a strong influence on

the aerodynamic drag. UAS with free spinning propellers can have up to 110% more drag compared to UAS with fixed propellers.

Further research may be required to investigate how the attitude of the UAS will change during a free fall. The presented drag coefficients and kinetic impact energies of each UAS can be transferred to the SORA process and used to improve the accuracy of ground risk class analysis.

**Acknowledgements** The authors like to express their gratitude to Siemens PLM Software for providing academic licenses of their software StarCCM+.

**Funding** Open Access funding enabled and organized by Projekt DEAL. Funding for this work was provided by the Department of Aerospace Engineering of FH Aachen University of Applied Sciences.

**Data availability** Not applicable.

**Code availability** Not applicable.

## Declarations

**Conflict of interest** The authors declare no conflict of interest to the content of this article.

**Open Access** This article is licensed under a Creative Commons Attribution 4.0 International License, which permits use, sharing, adaptation, distribution and reproduction in any medium or format, as long as you give appropriate credit to the original author(s) and the source, provide a link to the Creative Commons licence, and indicate if changes were made. The images or other third party material in this article are included in the article's Creative Commons licence, unless indicated otherwise in a credit line to the material. If material is not included in the article's Creative Commons licence and your intended use is not permitted by statutory regulation or exceeds the permitted use, you will need to obtain permission directly from the copyright holder. To view a copy of this licence, visit <http://creativecommons.org/licenses/by/4.0/>.

## References

1. European Union. COMMISSION IMPLEMENTING REGULATION (EU) 2019/947, 2019.
2. Hwang, M.H., Cha, H.R., Jung, S.Y.: Practical endurance estimation for minimizing energy consumption of multirotor unmanned aerial vehicles. *Energies* (2018). <https://doi.org/10.3390/en1092221>
3. Bannwarth, J.X.J., Jeremy Chen, Z., Stol, K.A., MacDonald, B.A., Richards, P.J.: Aerodynamic force modeling of multirotor unmanned aerial vehicles. *AIAA J.* (2019). <https://doi.org/10.2514/1.j057165>
4. Gloudemans, J., Davis, P., Gelhausen, P. *A rapid geometry modeler for conceptual aircraft*. 34th Aerospace Sciences Meeting and Exhibit, AIAA, Reston, VA, 1996. <https://doi.org/10.2514/6.1996-52>.
5. Götten, F. *Exploration and Development of New Drag Prediction Models for UAVs*. School of Engineering College of Science, Technology, Engineering and Maths RMIT University, 2021. <https://doi.org/10.13140/RG.2.2.14444.49286>
6. Quitter, J., Marino, M., Bauschat, J.-M.: Comparison of aerodynamic methods for flight mechanical derivative estimation of



- unconventional Aircraft. AIAA Scitech (2021). <https://doi.org/10.2514/6.2021-0324>
7. Spalart, P.R.: Strategies for turbulence modelling and simulations. *Int. J. Heat Fluid Flow* **21**(3), 252–263 (2000). [https://doi.org/10.1016/s0142-727x\(00\)00007-2](https://doi.org/10.1016/s0142-727x(00)00007-2)
  8. Spalart, P.R., Rumsey, C.L.: Effective inflow conditions for turbulence models in aerodynamic calculations. *AIAA J.* **45**(10), 2544–2553 (2007). <https://doi.org/10.2514/1.29373>
  9. Laurien, E., & Oertel, H., Jr. *Numerische Strömungsmechanik: Grundgleichungen und Modelle—Lösungsmethoden—Qualität und Genauigkeit*. Springer Science & Business Media, 2011.
  10. Mayntz, J., Keimer, J., Tegtmeier, P., Dahmann, P., Hille, S., Stumpf, E., Fisher, A., Dorrington, G.: Aerodynamic investigation on efficient inflight transition of a propeller from propulsion to regeneration mode. AIAA Scitech (2022). <https://doi.org/10.2514/6.2022-0546>
  11. : Gudmundsson, S. *General Aviation Aircraft Design: Applied Methods and Procedures*. Butterworth-Heinemann, 2016.

**Publisher's Note** Springer Nature remains neutral with regard to jurisdictional claims in published maps and institutional affiliations.